The GALAH survey: Lithium-rich giant stars require multiple formation channels

Sarah L. Martell,[1][*] Jeffrey D. Simpson,[1] Adithya G. Balasubramaniam,[1] Sven Buder,[2]
Simon W. Campbell,[3] Dennis Stello,[1,4,5] Sanjib Sharma,[5]
and all the GALAH coauthors[6]

[1]*School of Physics, UNSW Sydney, Sydney NSW 2052, Australia*
[2]*Research School for Astronomy & Astrophysics, Australian National University, Canberra, ACT 2611, Australia*
[3]*Monash Centre for Astrophysics, School of Physics and Astronomy, Monash University, Australia*
[4]*Centre of Excellence for All-Sky Astrophysics in Three Dimensions (ASTRO 3D), Australia*
[5]*Sydney Institute for Astronomy, School of Physics, A28, The University of Sydney, NSW, 2006, Australia*
[6]*etc*

ABSTRACT

We investigate the properties of 1306 evolved stars in the GALAH, K2-HERMES and TESS-HERMES surveys with high photospheric abundances of lithium, and discuss them in the context of proposed mechanisms for lithium enrichment in giant stars. Our red clump stars are mainly young and metal-rich, with orbits in the thin disc, while our red giant branch sample extends further into the halo. Using asteroseismic data from the *K2* mission together with GALAH+ DR3 stellar parameters, we find that 32.0 per cent of the lithium-rich giants in our data set are found on the red giant branch and 68.0 per cent on the red clump, similar to ratios found in recent literature. Red clump stars are more than three times as likely to be lithium-rich as red giant branch stars, while rapidly rotating red giant branch stars are nearly twice as likely to be lithium-rich as rapidly rotating red clump stars. There are striking differences in the occurrence rate with metallicity for lithium-rich red clump and red giant branch stars, a clear correspondence between rapid rotation and super lithium-richness on the red clump, and almost no stars on the secondary red clump with lithium abundances above the primordial level. The complex distribution of lithium-rich giants across evolutionary phase, metallicity and rotation rate imply multiple independent mechanisms for producing lithium enrichment.

Key words: stars:abundances – stars:evolution

1 INTRODUCTION

Lithium-rich giants have been a longstanding mystery in stellar evolution (Burbidge et al. 1957; Wallerstein & Conti 1969; Trimble 1975, 1991) since the first such evolved star was discovered by McKellar (1940, see their full description in McKellar 1941). Canonical stellar evolution predicts that a star with approximately Solar mass forms with the atmospheric lithium abundance that matches its local interstellar medium, and that abundance is preserved throughout the star's main sequence (MS) lifetime. The structure of MS stars, with radiative cores and fairly shallow convective envelopes, means that the material in the stellar atmosphere is never exposed to a high enough temperature to destroy the lithium (2.6×10^6 K; Gamow & Landau 1933; Salpeter 1955). Then, in the first dredge-up phase (Iben 1965), which happens as a star evolves from the MS to the red giant branch (RGB), the convective envelope deepens dramat-

ically. First dredge-up transports atmospheric material through the hot stellar interior, which subjects it to proton-capture fusion. This causes a sharp reduction in the surface abundances of lithium and carbon, and reduces the $^{12}C/^{13}C$ ratio (see, e.g., Gratton et al. 2000; Lind et al. 2009). As the star evolves along the RGB, there is a further sharp drop in photospheric lithium abundance at the luminosity bump. Then at the tip of the giant branch, the helium flash causes a rapid and dramatic reconfiguration of the star as it moves to the red clump (RC), establishing a helium-burning core and a much more compact atmosphere. There is not a clear and well-known effect on surface abundances due to the helium flash, though it is reasonable to expect light elements to be affected if there is any transport between the surface and the hydrogen-burning shell during this transition.

First dredge-up is a universal event in low-mass stellar evolution, and so we would expect to observe low photospheric lithium abundances in all red giant stars. However, a small fraction of giant stars, roughly one per cent (Gao et al. 2019), have high photospheric

lithium abundances, and some even exceed the primordial lithium abundance (e.g. Yan et al. 2018). Previous studies have uncovered a complex population of lithium-rich giants across a range of evolutionary phases and throughout the Local Group (references include Kraft et al. 1999; Pilachowski et al. 2000; Gonzalez et al. 2009; Kirby et al. 2016). While the first lithium-rich first-ascent red giant branch star was discovered in a globular cluster (Wallerstein & Sneden 1982), only a small number of additional lithium-rich globular cluster stars have been discovered. A fraction of lithium-rich giants exhibit features such as high rotational velocity (e.g., Charbonnel & Balachandran 2000), or infrared excess in their SED (e.g., Rebull et al. 2015), but as a rule they have not been observed to differ in any significant way from lithium-normal giants of the same stellar parameters and evolutionary phase (e.g., Martell & Shetrone 2013; Casey et al. 2016; Smiljanic et al. 2018; Deepak & Reddy 2019).

In response to the observational data, a number of mechanisms have been proposed for the acquisition, production, or preservation of lithium in evolved stars. These tend to focus on planet engulfment (e.g., Carlberg et al. 2012; Aguilera-Gómez et al. 2016) or internal mixing in conjunction with the Cameron & Fowler (1971) lithium production process (e.g., Charbonnel & Balachandran 2000; Denissenkov 2012; Casey et al. 2019). The models are often closely tied to particular events in stellar evolution.

More recent work has identified that lithium-rich giants are more likely to be in the red clump (i.e., core-helium burning stars) than on the first ascent red giant branch (i.e., hydrogen-shell burning stars). To evaluate arguments about the source of lithium enrichment it is critical to know the evolutionary phase of the stars in question. It can be difficult to confidently separate red clump stars from red giant branch stars with similar surface gravity based on photometry or stellar parameters. Asteroseismology has the potential to provide crucial perspective on this problem, as asteroseismic parameters are clearly distinct for RGB stars with degenerate hydrogen cores and RC stars with helium burning cores (Bedding et al. 2011).

With the availability of lithium abundances from large spectroscopic projects like the *Gaia*-ESO Survey (Gilmore et al. 2012), the LAMOST survey (Cui et al. 2012), and the GALAH Survey (Buder et al. 2018), and the tremendous expansion in asteroseismic sky coverage from the *K2* (Stello et al. 2017) and *TESS* (Silva Aguirre et al. 2020) missions, we can now assemble and use large catalogues of lithium-rich giants with reliably determined evolutionary states. Recent works (Singh et al. 2019; Gao et al. 2019; Casey et al. 2019; Deepak & Reddy 2019; Deepak 2020) have identified thousands of lithium-rich giants in the Milky Way, a major expansion from the previous small samples.

The goal of this study is to expand the parameter space of the study of lithium-rich giants. The GALAH+ Survey provides a large initial set of red giant stars (described in Section 2). Using this data set we make use of a reliable classification of red giant branch and red clump stars using a Bayesian isochrone classification scheme (Section 2.4). We investigate the bulk properties of lithium-rich giant stars, including the distribution in evolutionary phase and the occurrence rate as a function of metallicity (Section 3.1) and other elemental abundances (Section 3.2); we consider observational factors discussed in previous studies including rotational velocity (Section 3.3), binarity (Section 3.5), and infrared excess (Section 3.6); we are able to explore the Galactic kinematic properties of the stars (Section 3.4), to investigate how lithium-rich giants are distributed across Galactic populations. Finally, we discuss our findings and make the case that there are multiple pathways for lithium enrichment in giant stars (Section 4)

2   THE DATA SET

In this section we describe the overall data set (Section 2.1), our giant star selection (Section 2.2), lithium abundance determination (Section 2.3), and classification of stellar evolutionary phase (Section 2.4).

2.1   Observation, reduction, and analysis

Our data set of 566919 stars comes from the merger of the results of the GALAH survey (De Silva et al. 2015; Buder et al. 2018), the *K2*-HERMES survey (Wittenmyer et al. 2018; Sharma et al. 2019) and the *TESS*-HERMES survey (Sharma et al. 2018) — the combination of these three surveys is referred to in this work as the GALAH+ survey. All three of these projects use same instrumental setup — the HERMES spectrograph (Sheinis et al. 2015) with the 2dF fibre positioning system (Lewis et al. 2002) at the 3.9-metre Anglo-Australian Telescope — to take high-resolution ($R \sim 28000$) spectra for stars in the Milky Way. HERMES records ~ 1000 Å across four non-contiguous sections of the optical spectrum, including the region around the Hα line, which contains the lithium resonance line at 6708 Å.

Each input survey has its own selection function. The main GALAH survey (74 per cent of the data set) uses a simple selection function to acquire a data set from which the underlying properties of the Milky Way can be straightforwardly interpreted: the target catalogue consists of all stars with $12 < V < 14$ and $|\delta| < 10$ deg in regions of the sky that have at least 400 targets in π square degrees (the 2dF field of view). The *K2*-HERMES survey (16 per cent of the data set) is the spectroscopic data corresponding to the *K2* Galactic Archaeology Program (Stello et al. 2017), and is therefore weighted toward red giant stars for which Solar-like oscillations can be measured in *K2* time-series photometry. The *TESS*-HERMES survey (3 per cent of the data set) was undertaken to assist the target selection for the *TESS* mission by providing stellar parameters for *TESS* targets more precisely than can be done photometrically (Sharma et al. 2018; Stassun et al. 2019). Those observations focused on stars in the *TESS* apparent magnitude range ($10 < V < 13.1$) in the *TESS* continuous viewing zone within 12 degrees of the Southern ecliptic pole. The remaining 3 per cent of the data set consists of open cluster and globular cluster targets that were not part of either of these surveys.

The HERMES data from all three surveys are reduced with the same custom IRAF pipeline, which is described in Kos et al. (2017), and analysed with the Spectroscopy Made Easy (SME) software (Valenti & Piskunov 1996; Piskunov & Valenti 2017). The analysis is described in detail in Buder et al (2020, in prep), but briefly, it uses SME to perform spectrum synthesis for 1D stellar atmosphere models. We use MARCS theoretical 1D hydrostatic models (Gustafsson et al. 2008), with spherically symmetric stellar atmosphere models for $\log g \leq 3.5$ and plane parallel models otherwise. SME carries out radiative transfer under the assumption of local thermodynamic equilibrium, and so we incorporate non-LTE line formation for elements (including lithium, Lind et al. 2009) where the effect on abundance determination is known to be significant. In all cases the non-LTE computations are performed using the same grid of MARCS model atmospheres as the LTE computations.

2.2   Giant star selection

For this work, we are using the GALAH+ Data Release 3 catalogue of stellar parameters and abundances. At the time
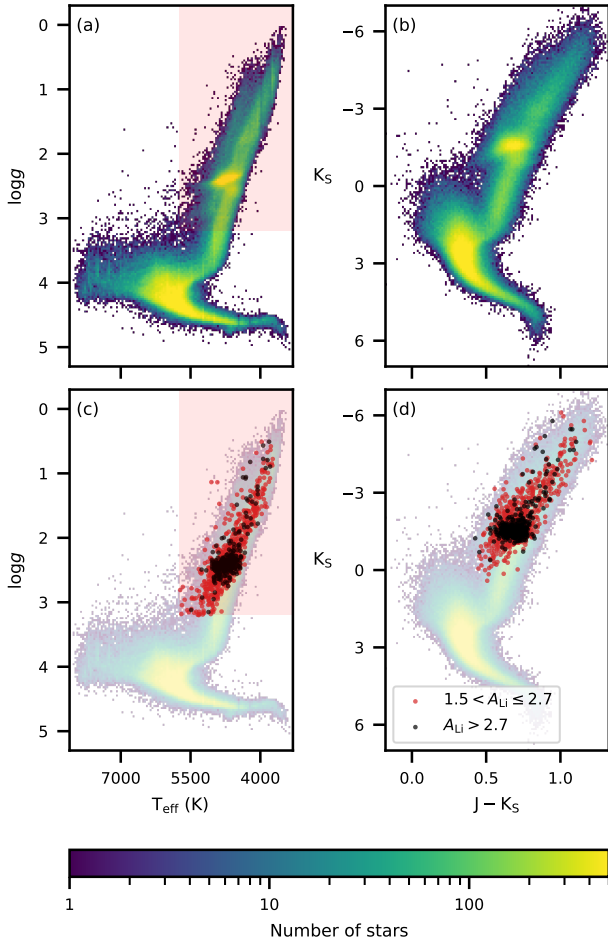
Figure 1. Kiel diagrams (left column) and absolute colour-magnitude diagram (right column) for the "good" sample (i.e., no flagged problems) of GALAH+ stars considered in this work. The red rectangle in (a) and (c) shows the T_{eff}, log g selection used to identify giant stars. In the bottom row we highlight giant stars with $A_{Li} > \{1.5, 2.7\}$, using red and black points respectively. This shows that Li-rich giants are found at all parts of the giant branch, but the very Li-enhanced stars ($A_{Li} > 2.7$) tend to be found in the red clump region.

of writing this catalog is internal, and it will be publicly released in mid-2020[1]. This contains 566919 stars that are also in the *Gaia* DR2 (Gaia Collaboration et al. 2016, 2018) and *All-WISE* (Wright et al. 2010; Mainzer et al. 2011) catalogues. This cross-match used the `gaiadr2.allwise_best_neighbour` and `gaiadr2.tmass_best_neighbour` tables created by the *Gaia* mission team.

We apply a number of quality and parameter cuts to identify our sample of reliable lithium-rich giant stars. We excluded stars known to be in the SMC or LMC based on their spatial and kinematic properties. We required that each star has:

- the GALAH flag `flag_sp == 0`: no problems noted in the input data, reduction, or analysis;
- the GALAH flag `flag_fe_h == 0`: no problems noted in the iron abundance determination;

---

[1] A link to the public data will be available from galah-survey.org

- a calculated $E(B - V) < 0.33$;
- a photometric measurement in the *WISE* W_2 band.

These criteria retained 66.9 per cent (379318/566919) of the sample as "good" stars. Kiel and colour-magnitude diagrams of these stars are shown in Figure 1.

Secondly, we obviously restrict ourselves to giant stars, with those stars found to have effective temperature in the range 3000 K $\leq$ $T_{eff} \leq$ 5730 K and the surface gravity in the range 3.2 $\geq$ log g $\geq$ −1.0. Of our sample of "good" stars, 31.6 per cent (120024/379318) were identified as giant stars.

2.3 Lithium abundances

The lithium abundance of each star was determined as part of the main analysis of the GALAH+ spectral data set from synthesis of the 6708 Å lithium line. We report the lithium abundance value in the form of $A_{Li} (\equiv [Li/Fe] + [Fe/H] + 1.05)$, where the A_X abundance scale gives the number density of element X on a logarithmic scale relative to hydrogen, with $A_H = 12$ by definition and 1.05 as the lithium abundance of the Sun (Asplund et al. 2009). We follow the typical convention from the literature of considering a giant star to be lithium-rich if its abundance A_{Li} is greater than 1.5 (see discussion in Kirby et al. 2016, on whether this Li-rich limit should be a function of stellar parameters). We also highlight throughout this work the subset of these Li-rich giant stars with A_{Li} above the primordial value of 2.7 (Cyburt et al. 2008; Fields et al. 2020).

Of the 120024 "good" giant stars, only 10828 (9.0 per cent) had a measured A_{Li} in the GALAH+ catalogue (defined as having `flag_li_fe == 0`; i.e., no flagged problems with the [Li/Fe] determination). As with any spectral line, the strength of the lithium line is a complicated function of the stellar parameters and the lithium abundance of the star. In Figure 2 we show example HERMES spectra for giant stars of similar [Fe/H] across the range of T_{eff} and log g values on the red giant branch. Each panel shows spectra for 11 randomly selected stars with similar stellar parameters, of which one has a lithium abundance $A_{Li} \sim 2.3$. This highlights that for most stars, the 6708 Å line of lithium is not detectable, and that the sensitivity to lithium abundance decreases as T_{eff} rises. This explains why only 9 per cent of our giant star sample has a measured value for A_{Li} despite high quality spectra.

Very high lithium abundances are also challenging for our abundance pipeline to determine correctly. Above an abundance of $A_{Li} \approx 4.6$, the curve of growth for the 6708 Å line is quite flat, such that small changes in line strength imply large changes in abundance. All spectral lines in GALAH that are in this regime approaching saturation are flagged as unreliable, and as a result, there may be even lithium-richer stars that do not have catalogue abundances. These stars will require bespoke analysis for accurate abundance determination.

For our giant star sample, 1306/120024 (1.1 per cent) have $A_{Li} > 1.5$. This is consistent with the 1.29 per cent value found independently in the LAMOST survey (Gao et al. 2019). Of our 1306 Li-rich giants, 329 stars lie above the primordial value of $A_{Li} = 2.7$. The location of our Li-rich giants in the Kiel diagram is shown in Figure 1.

On the lower giant branch (log g $\sim$ 3), there is a dearth of Li-rich stars on the cooler side of the giant branch. This is a combination of two effects: firstly, the already discussed detectability limit on the lithium line available in the HERMES spectra (see also Section 3.1 and Figure 4); and secondly, the deeper surface convective envelopes of cooler stars, which extend to hotter layers in the stellar interior and

Table 1. We identify 1306 Li-rich giants with reliable evolutionary stage classifications. Here we give their Gaia DR2 `source_id`, sky locations, and GALAH+ stellar parameters and spectroscopic information. The full version of the table is available online; the six entries included here are the Li-rich stars shown in Figure 2.

| source_id	RA	Dec	RV (km s^{-1})	T_{eff} (K)	log g	[Fe/H]	A_{Li}	RC or RGB
6137526858900209920	199.020	−41.767	−24.42 ± 0.29	3970 ± 72	1.63 ± 0.22	−0.17 ± 0.05	2.25 ± 0.06	RGB
5371899834025124608	175.501	−48.171	1.43 ± 0.66	4285 ± 158	1.75 ± 0.26	−0.22 ± 0.17	2.21 ± 0.23	RGB
6100901881763791232	223.933	−42.034	−18.00 ± 0.33	4429 ± 80	2.01 ± 1.20	−0.18 ± 0.05	2.40 ± 0.08	RGB
6235140814020759808	236.883	−25.259	−23.43 ± 0.55	4681 ± 127	2.31 ± 0.26	−0.18 ± 0.11	2.25 ± 0.16	RC
6129493448995721984	180.111	−50.437	−50.04 ± 0.33	4980 ± 80	2.55 ± 0.21	−0.21 ± 0.05	2.25 ± 0.08	RC
3155263089390175872	109.992	9.198	38.66 ± 0.58	5147 ± 127	2.72 ± 0.24	−0.18 ± 0.11	2.29 ± 0.16	RC
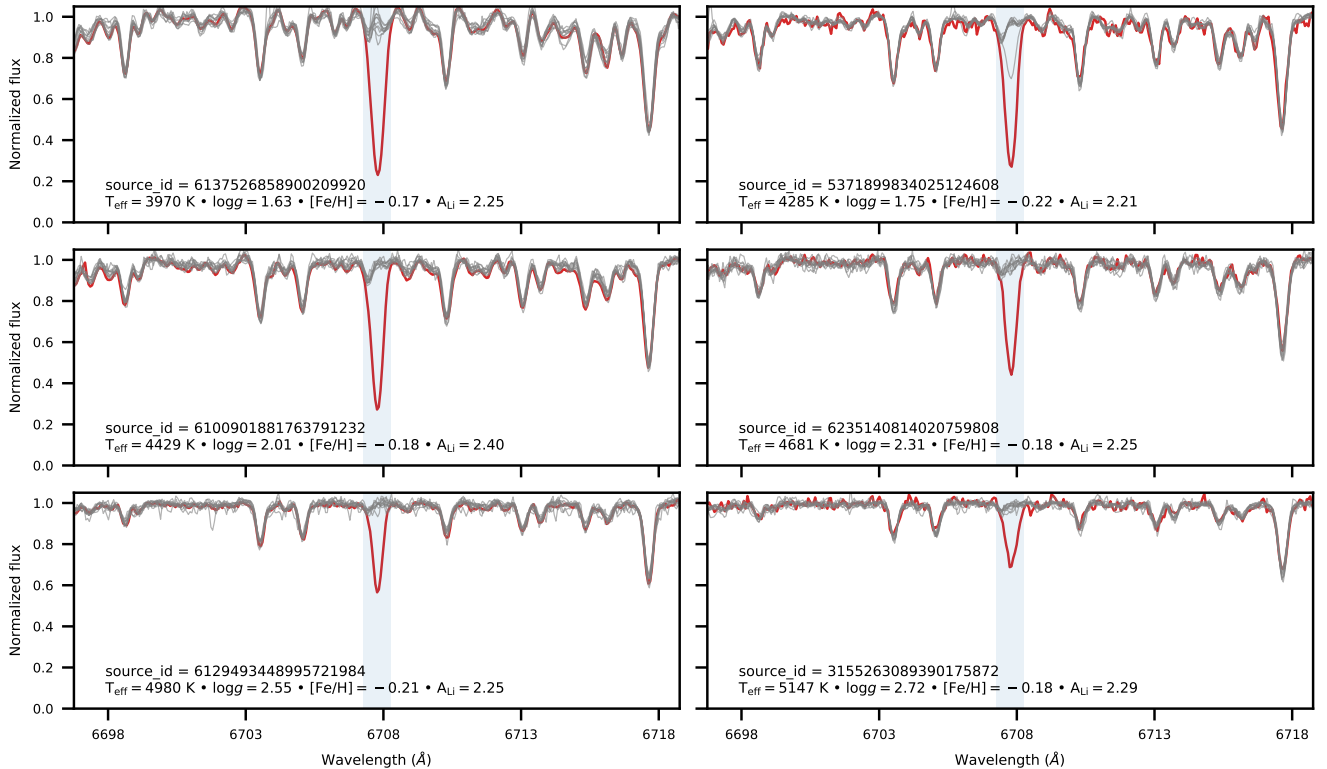
Figure 2. Examples of the spectral region containing the Li 6708 Å line (indicated with the shaded blue region in each panel), as observed with HERMES, for stars from a range of T_{eff} and log g along the giant branch. In each panel we highlight one Li-rich giant star (red line) and 10 other randomly selected stars with similar stellar parameters (grey lines) — namely $\Delta(T_{eff}) < 50$ K, $\Delta(\log g) < 0.2$, $\Delta([Fe/H]) < 0.03$, $\Delta([\alpha/Fe]) < 0.05$, $v_{broad} < 5$ km s^{-1}. In all panels, the Li-rich stars have approximately the same metallicity and A_{Li}. There are two things to note: first, for most of the stars, the lithium line is either a weak or not visible; second, for a given A_{Li}, the lithium absorption line gets weaker with increasing T_{eff}— which means that at higher temperatures the minimum detectable A_{Li} is higher.

allow for more depletion of the surface lithium abundance (Ramírez et al. 2012; Buder et al. 2018).

2.4   Classifying evolutionary phase

The evolutionary state of lithium-rich giants is an essential piece of knowledge for evaluating models to explain their enrichment. The GALAH+ survey observes two main populations of low-mass giants in the Milky Way:

- Red giant branch (RGB) stars, on their first ascent of the giant

branch, with an inert helium core and a hydrogen-burning shell. The RGB spans a wide range in log g and luminosity.

- Red clump (RC) stars, in the stage directly after the first ascent of the giant branch, with a helium-burning core and a hydrogen-burning shell. RC stars occupy only a small range of He-core mass and therefore luminosity, and they fall near RGB stars with the same log g in the observable parameter space.

About one-third of evolved stars in a magnitude-limited survey are expected to be RC stars (Girardi 2016). However, as noted by many authors (Casey et al. 2019; Zhang et al. 2020; Gao et al. 2019), Li-rich giants are more likely to be RC stars than RGB. As shown

Table 2. Comparison of the classifications of the RC and RGB stars using Hon et al. (2019) and our BSTEP+photometry selection, with recovery and misclassification rates included. As an example, 568 stars were classified as RC stars using their seismic information and 510 of these 568 were classified as RC stars using BSTEP: a 90 per cent recovery rate. Conversely, 654 stars were classified as RC by BSTEP, and the same 510 of these were classified as RC from seismic information: 78 per cent.

	RC (BSTEP)	RGB (BSTEP)	Total
RC (seismic)	510 (78%; 90%)	58 (17%; 10%)	568
RGB (seismic)	144 (22%; 34%)	278 (83%; 66%)	422
Total	654	336	990

in the bottom row of Figure 1, there is a clear over-density of stars corresponding to the location of the red clump, both for the Li-rich and super-Li-rich stars.

As discussed in Section 1, RC and RGB stars can be distinguished using asteroseismology. The ability to infer the interior properties of stars has been greatly improved by the precise photometry recorded by various space missions (e.g., *CoRoT*, *Kepler*, *K2*, *TESS*). The gravity period spacing ($\Delta\Pi$) and the large frequency spacing ($\Delta\nu$) can be measured from the power spectra derived from these light curves, and these quantities take very different distributions for red clump and red giant branch stars (e.g., Mosser et al. 2012; Stello et al. 2013; Vrard et al. 2016). This technique has been used for small samples of Li-rich giants to get unambiguous classifications (Singh et al. 2019; Casey et al. 2019).

Most of our giant stars do not have the necessary time-series photometry. The time series photometry in *K2* and *TESS* is not as extensive as it was for the original *Kepler* mission, making derivation of $\Delta\Pi$ quite difficult. However, classification of red clump versus red giant branch stars can be done reliably from *K2* data. We took classifications for *K2* stars in our sample from Hon et al. (2019), who use a convolutional neural network with images of the power spectra to classify RC vs RGB stars with 99% reliability. 990 of the K2 stars in our sample have reliable stellar parameters and seismic classifications from this technique. Of these, 568 stars are classified as RC and 422 are RGB, but only 8 of the 990 stars are lithium-rich. We indicate these stars throughout this work, but do not rely on them for any of the conclusions.

Therefore, for the majority of our stars we used RGB/RC classifications from the Bayesian Stellar Parameters estimator (BSTEP). This is described in detail in Sharma et al. (2018), but briefly, it provides a Bayesian estimate of intrinsic stellar parameters from observed parameters by making use of stellar isochrones. For results presented in this paper, we exploit the PARSEC-COLIBRI stellar isochrones (Marigo et al. 2017). We supplement these classifications by taking advantage of the fact RC stars are standard candles. The WISE W_2 absolute magnitude of the stars was calculated using the conventional relationship $M_\lambda = m_\lambda - 5\log(r_{est}) + 5$, with the distance r_{est} taken from Bailer-Jones et al. (2018). The vast bulk of our RC stars were found in the range $W_2 = -1.63 \pm 0.80$, in line with expectations (Karaali et al. 2019; Plevne et al. 2020). Our RC and RGB selections are made as follows:

• RC stars: BSTEP RC probability ≥ 0.5 and absolute magnitude in the range $W_2 > -1.63 - 0.80$,
• RGB stars: BSTEP RC probability < 0.5 or absolute magnitude outside the range $W_2 \leq -1.63 - 0.80$.
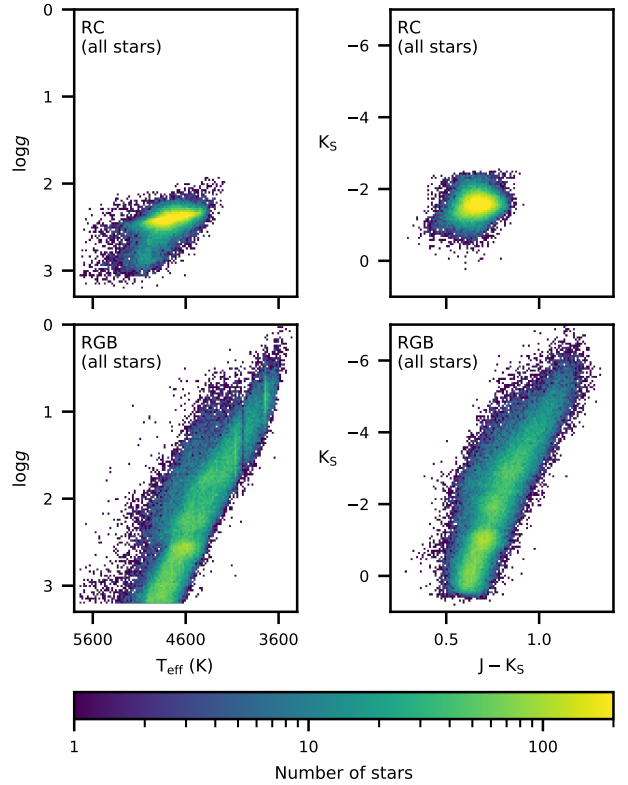
Figure 3. Kiel diagrams (left column; T_{eff} vs $\log g$) and absolute colour-magnitude diagrams (right column) for the stars selected to be from (top row) RC, and (bottom row) RGB. For the RC stars there both the primary RC and the higher $\log g$ secondary RC can be seen. In the RGB panels the region of higher density on the lower giant branch is the RGB bump.

In Table 2 we compare the results from the seismic and isochrone-based BSTEP classifications. Considering, for instance, the red clump stars, the BSTEP classification recovers 90 per cent (510/568) of red clump stars identified from asteroseismology. For the RGB stars this recovery rate is 66 per cent. Conversely, of the 654 stars classified as RC stars by BSTEP, 22 per cent (144/654) were classified as RGB stars by the seismic method. Similarly, of the 336 BSTEP RGB stars, 17 per cent (58/336) were seismic RC stars. The similar false positive and false negative rates for RGB and RC stars in Table 2 indicate that the RC classification is more secure, given the unambiguous classification of low-gravity RGB stars.

Using the BSTEP classification of RC and RGB stars for our full set of 120024 giants, 44767 (37.3 per cent) are on the RC, and 75257 (62.7 per cent) belong to the RGB — as expected for a magnitude-limited survey (Girardi 2016). These results are presented in Figure 3 and in Table 3. The expected morphologies in the Kiel and absolute colour-magnitude diagrams are recovered; namely, in the Kiel diagram, the RC shows the primary red clump, and also the secondary red clump that consists of slightly more massive stars; and the RGB shows evidence for the luminosity function bump at a slightly higher $\log g$ than the bulk of the RC.

If we consider just the sample of 1306 Li-rich giants, 888 (68.0 per cent) are on the RC, and 418 (32.0 per cent) are on the RGB. It three times more likely for an RC star to be Li-rich (888/44767; 2.0 per cent) than for an RGB star to be Li-rich (418/75257; 0.6 per cent), a statistic that has not been reported previously.

Table 3. Counts of RGB and RC stars from our BSTEP classification, and the number of stars that are Li-rich ($A_{Li} > 1.5$) and super Li-rich ($A_{Li} > 2.7$). RC stars are divided into the primary RC (pRC) and secondary RC (sRC) at stellar mass of 1.7 solar masses (estimated using the same BSTEP method). The first percentage shows the proportion with respect to that of the total population of that type — e.g., for Li-rich RC stars, $888/1306 = 68$ per cent. For columns with a second percentage, this shows the percentage of the previous column value, e.g., there are 75 super Li-rich RGB stars, which is 18 per cent of the total number of Li-rich RGB stars (418).

Star type	Total stars	Li-rich	Super Li-rich
All giants	120024	1306 (1%)	329 (25%)
RC	44767 (37%)	888 (68%; 2%)	254 (77%; 29%)
pRC	41304 (34%)	763 (58%; 2%)	244 (74%; 32%)
sRC	3463 (3%)	125 (10%; 4%)	10 (3%; 8%)
RGB	75257 (63%)	418 (32%; 1%)	75 (23%; 18%)

3 LITHIUM-RICH GIANTS AS A STELLAR POPULATION

In this section we compare and contrast Li-normal and Li-rich giants in the fundamental stellar parameters T_{eff}, log g and [Fe/H] (Section 3.1), elemental abundances (Section 3.2), rotation rates (Section 3.3), stellar kinematics (Section 3.4), binarity (Section 3.5), and infrared excess (Section 3.6).

3.1 Lithium-rich giants across the fundamental stellar parameter space

Figure 4 presents the A_{Li} for our giants with respect to their basic stellar parameters: T_{eff}, log g, [Fe/H]. The upper row shows only red clump stars, and the lower row shows only red giant branch stars. The same stars are shown in all three columns, and stars with asteroseismic classifications are represented with star shapes. Horizontal lines mark the typical definition of "lithium-rich" at A_{Li} = 1.5 and the primordial lithium abundance, A_{Li} = 2.7.

There is a T_{eff}-dependent lower envelope to the lithium abundance that can be measured for giant stars in GALAH+, which is a result of a weaker 6708 Å resonance line at higher T_{eff}, for a fixed A_{Li} — see the spectra plots in Figure 2 and discussion in Section 2.3. It is possible that we are missing some of the hotter Li-rich giants.

As shown in Figure 3, the red clump stars observed by GALAH are split into two main populations: the lower gravity primary RC (pRC) and the higher gravity secondary RC (sRC). In Figure 4 they are most readily distinguished in the top-middle panel, where to aid the reader, there is a vertical line at log g = 2.7 that roughly separates the sRC from the pRC. Of particular note is that only a handful of stars on the sRC are super Li-enriched ($A_{Li} > 2.7$). As shown in Table 3, using the mass calculated by BSTEP for each star, the RC sample is split at a mass of 1.7 solar masses (Girardi 2016), there are 3463 sRC stars, of which 125 are Li-rich, but only 10 of these are super Li-rich — 0.3 per cent of sRC stars and 8.0 per cent of Li-rich sRC stars. Meanwhile, there are 41304 pRC stars, of which 763 are Li-rich, and 244 are super Li-rich (0.6 per cent; 31.9 per cent). This indicates that the mass of an RC star is an important part of whether it becomes Li-rich.

The RGB luminosity function bump plays two important roles in the study of Li-rich giants: a sudden drop in surface lithium abundance has been observed in stars at the bump (Lind et al. 2009),

and it has been invoked as a potential site of lithium production (Charbonnel & Balachandran 2000). There does appear to be a dearth of Li-rich RGB stars at the high-gravity end of the RGB star distribution. However, this picture is complicated, as stars below the RGB bump will also be hotter and therefore closer to the lithium detectability limit.

The right column of Figure 4 shows the behaviour of A_{Li} with metallicity for our giant stars, separated into the RC and RGB populations. The RC cohort clearly lacks stars with [Fe/H] < −1, which is to be expected for red clump stars in the Milky Way — there is a minimum mass for RC stars, and as a result they are a moderately young and metal-rich population (e.g., Ramírez et al. 2012). The evolution of metal-poor RC stars is also faster than for more metal-rich stars (Girardi 2016), making them less likely to be observed.

The metal-poor RGB stars are almost exclusively below the Li-rich threshold, with a concentration at $A_{Li} \approx 1.0$. These stars are mainly located near the luminosity function bump, indicating that first dredge-up has reduced their A_{Li} abundance to around 1, and that it will continue to fall as they evolve along the RGB.

There has been some tension in the literature between the < 1 per cent occurrence rates of Li-rich giants in the low metallicity environments of globular clusters (where our sampling can be much more complete, see e.g., Kirby et al. 2012), and the > 1 per cent rate observed in the disk of the Milky Way. Recent works with larger data sets (e.g., Casey et al. 2019; Deepak et al. 2020) have quantified this as a more general increase in occurrence rate with increasing metallicity. In Figure 5 we consider the occurrence rate of Li-rich giants with metallicity in our RC and RGB cohorts independently. The uncertainty of each bin in the histogram was calculated from 1000 bootstrap samples of the iron abundance values. The metallicity distribution of the Li-rich giants is qualitatively similar to the distribution for all giants. As would be expected for the GALAH+ sample, which is comprised mainly of Galactic disc stars, the distribution peaks near solar metallicity. For the RGB sample there is a tail of stars to low metallicity.

The occurrence rate of Li-rich giants in both groups rises at high metallicity, but the distributions are quite different. For the RC stars there is a steady increase of occurrence rate with metallicity, while for RGB stars, the occurrence rate is relatively flat from −2 < [Fe/H] < 0, and then increases dramatically for stars with super-solar metallicity (though with larger error bars due to the smaller number of stars observed at these metallicities). We interpret this increase as a sign of multiple lithium enrichment processes at work, with the dominant mechanism for red clump stars being quite sensitive to stellar metallicity, the dominant process for RGB stars with sub-solar metallicity being independent of metallicity, and potentially a third lithium enrichment process for (presumably young) metal-rich RGB stars.

3.2 Other elemental abundances in Li-rich giants

The abundances of other elements in Li-rich giants could provide information about the processes by which the lithium abundance of some giants is enhanced. GALAH+, with its wide range of elements from a variety of nucleosynthetic pathways, gives a great opportunity to explore this.

Interestingly, there are only a few elements in GALAH+ DR3 that show any obvious differences between the abundance patterns of Li-normal and Li-rich giants. In this section we discuss [α/Fe] (and the elements that form our α sum; Section 3.2.1) and [C/Fe]

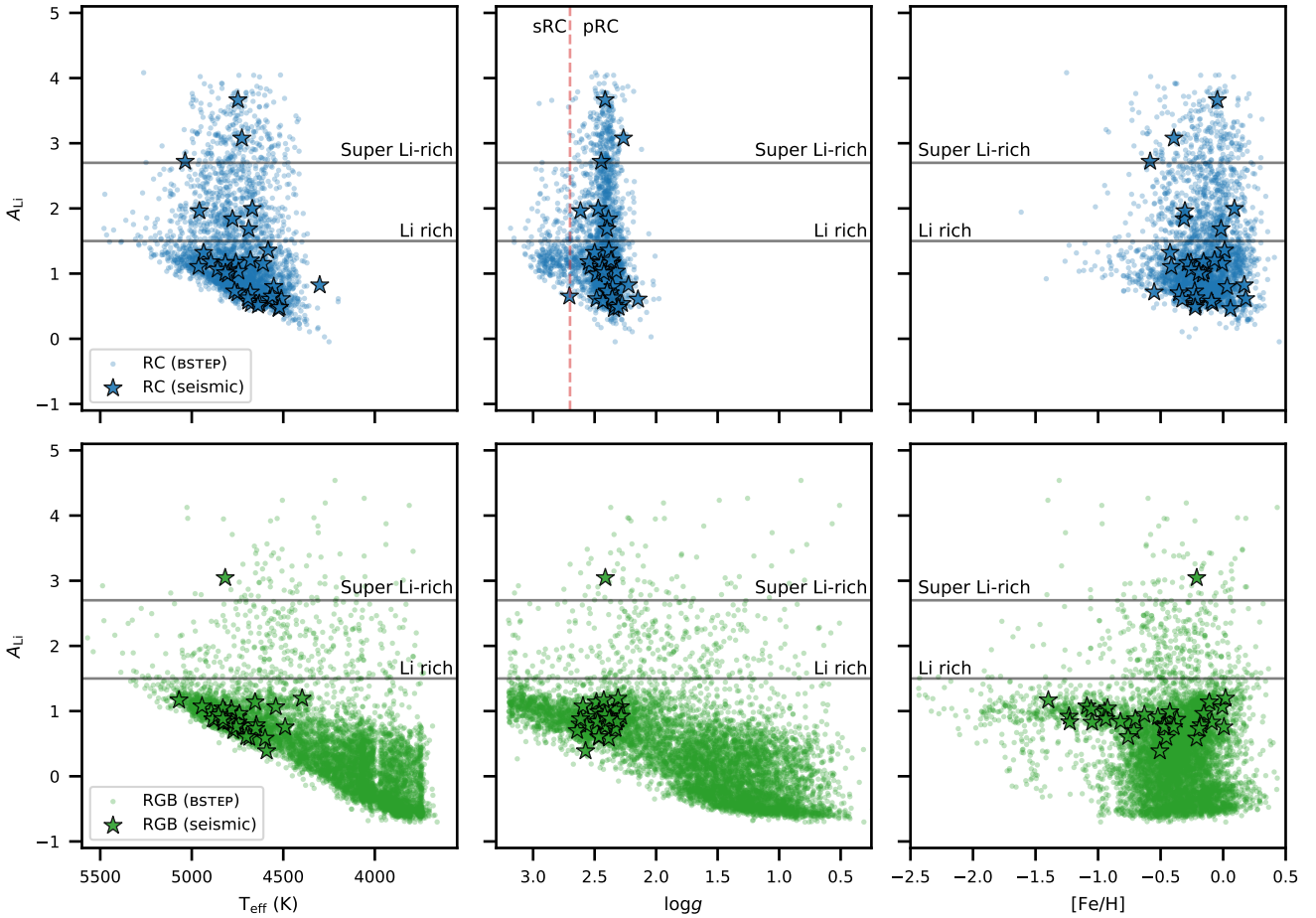**Figure 4.** Comparing the A_{Li} abundances with respect to T_{eff} (left column), log g (middle column), and [Fe/H] (right column). These are split into the red clump sample (upper panel of each column) and red giant branch sample (lower panel of each column). In all panels we show the stars classified as RC or RGB by the isochrone-based BSTEP method (dots) and the asteroseismic classifications (black-edged star symbols). The horizontal lines in all panels indicate criteria for whether a star is Li-rich or super Li-rich. In the T_{eff} panels there is a clear lower envelope in A_{Li}, indicating a detectability limit driven by line strength. In the log g panel for RC stars (upper middle) we highlight the regions occupied by the secondary red clump (sRC) and primary red clump (pRC) to note the lack of super Li-rich sRC stars. In the [Fe/H] RC panel there is a distinct lack of Li-rich stars with [Fe/H] < −1, which is real and not a matter of sensitivity to lithium line strength.

(Section 3.2.2), as this was recently highlighted by Deepak et al. (2020) as showing possible correlations with lithium enrichment.

3.2.1 Alpha elements

For GALAH+ DR3, [α/Fe] is the error-weighted combination of selected Mg, Si, Ca, and Ti lines. As Figure 6 shows, the [α/Fe] distribution of the Li-normal and Li-rich giants tracks much the same. However, we find that the super Li-rich RC stars have a clear preference for low α enhancement.

We do not think that this is because the lithium enrichment process destroys α elements, or is hampered by their presence. Rather, it is a function of the Galactic components that are captured in our observational sample. The RGB stars we observe can have much higher luminosities than the RC stars, and they are drawn from a larger volume, including more of the thick disk and the halo. The overall set of RC stars, being more restricted to the Solar neighbourhood, are more likely to have high metallicity and low α enhancement. The fact that the super Li-rich RC stars are more

skewed toward the metal-rich, α-poor group than RC stars in general indicates that metallicity plays some role in the process that produces super Li-rich RC stars.

3.2.2 Carbon

Deepak et al. (2020) recently explored the other elemental abundances of Li-rich and Li-normal giants using the GALAH DR2 data set. They found that for all the elements available, the only element that showed an appreciable difference between the two populations was carbon. Unfortunately, this result relied upon abundances that had been identified by the GALAH team as unreliable (i.e., the quality flags on the abundances were non-zero). Figure 7 shows the non-flagged (i.e., reliable) carbon abundances of RC and RGB stars in GALAH+ DR3. The spectroscopic features of carbon captured in HERMES spectra are quite weak in the bulk of giant stars, and therefore our sensitivity to [C/Fe] is limited. This produces a clear detectability trend that can be seen in the figure, where lower carbon abundances are only detected for more metal-rich stars.
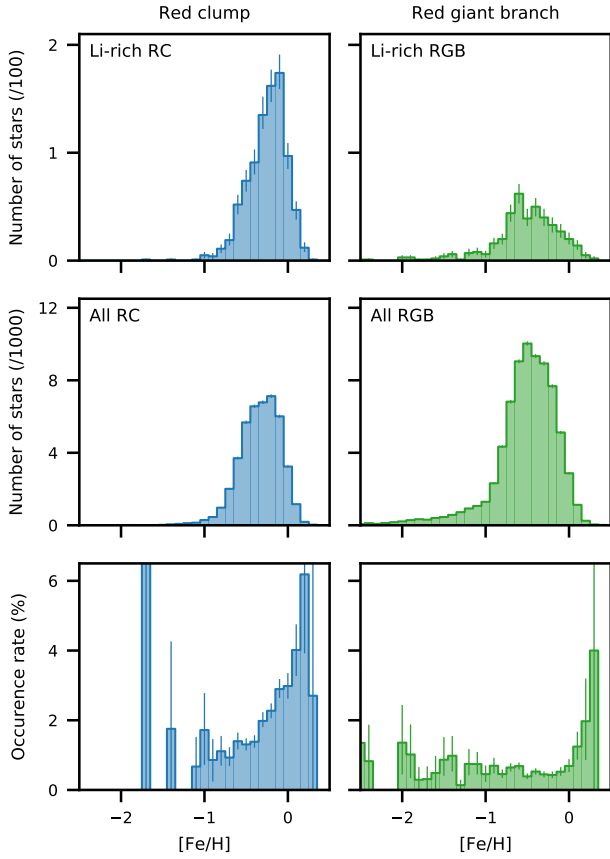
Figure 5. Comparing the occurrence rate of Li-rich giants with changing [Fe/H] for the RC (left column) and RGB (right column) cohorts (here just showing the BSTEP classification method results). In the top panel of each column is the [Fe/H] distribution of Li-rich giants from each cohort; the middle panel is the [Fe/H] distribution of all stars each cohort (whether or not they have a measured A_{Li}); and the bottom panel of each column is the occurrence rate with [Fe/H] (i.e, the top panel 'divided' by the middle panel). The uncertainty of each bin in the histogram was calculated from 1000 bootstrap samples of the iron abundance values. The occurrence rate of Li-rich giants in both groups rises at high metallicity, but the distributions are quite different — for the RC stars there is a steady increase of occurrence rate with metallicity, while for RGB stars, the occurrence rate is relatively flat below [Fe/H] = 0.

Interestingly, we do derive reliable (and high) carbon abundances for a number of stars. First dredge-up and subsequent mixing processes typically result in sub-solar [C/Fe] for giant stars (e.g., Lagarde et al. 2019). Carbon-richness at this stage in stellar evolution often indicates mass transfer from an asymptotic giant branch (AGB) companion, and may be accompanied by other chemical tags of AGB nucleosynthesis including s-process elements (e.g., Hansen et al. 2016; Karakas & Lugaro 2016). The topic of carbon-enhanced giant stars in GALAH+ DR3 is outside the scope of this paper, but bears further investigation.

3.3 Stellar rotation

The rotation rates of our stars is of interest because one of the proposed modes of lithium enhancement is rotationally induced mixing,
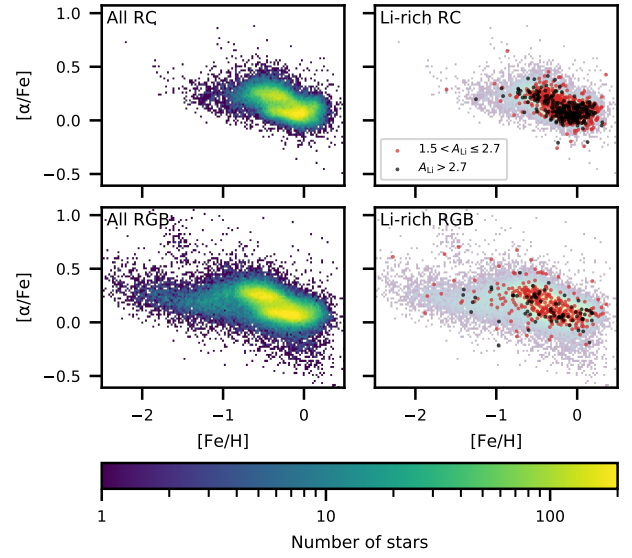
Figure 6. Comparison of the [α/Fe] abundances of the RC (top row) and RGB (bottom row) stars. In the right column we further highlight the Li-rich (red dots) and super Li-rich (black dots) giants. For the RC stars, we find that the majority of super Li-rich giants belong to the α-poor 'thin disc' population.
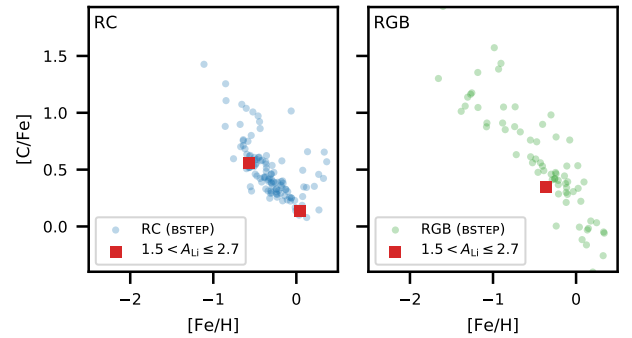

Figure 7. Carbon abundance [C/Fe] for the RC (left) and RGB (right) stars. Carbon can only be measured in HERMES spectra for a small minority of giant stars where it is abundant. The carbon abundance of Li-rich giants is of interest because the two elements are depleted together during first dredge-up, and carbon may also be destroyed by fusion processes at temperatures that can destroy lithium. Only three of the Li-rich giants (all with $1.5 < A_{Li} \leq 2.7$) have a measured [C/Fe], and they follow the A_{Li} behaviour of the other stars with measured [C/Fe].

which can raise the surface lithium abundance via the Cameron & Fowler (1971) process.

As part of the spectroscopic analysis in GALAH+, an overall spectral broadening parameter v_{broad} is calculated, which encompasses microturbulence, macroturbulence and rotational velocity. Typically in RGB stars, the microturbulence velocity is on the order of $1 \ km\,s^{-1}$ and the macroturbulence velocity is on the order of $7 \ km\,s^{-1}$ (Carney et al. 2008b). So we can interpret stars of large v_{broad} as having a large rotational velocity component.

In Figure 8 we show the distributions of v_{broad} with log g for RC and RGB stars separately. As expected v_{broad} increases in
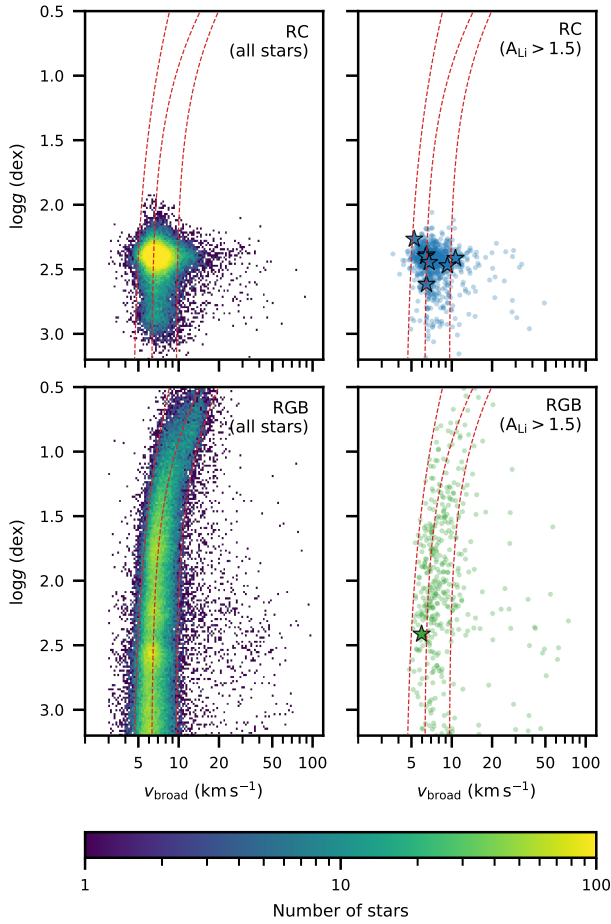
Figure 8. The v_{broad} distributions of the red clump (top row) and red giant branch (bottom row) samples. The quantity v_{broad} is a broadening term measured from the stellar spectra that encompasses microturbulence, macroturbulence and rotational velocity. The left column shows all giants from the RC and RGB cohorts, while the right column shows just the Li-rich stars ($A_{Li} > 1.5$). As in Figure 4, in the right column we highlight the stars identified seismically as RC or RGB with open star shapes. On all panels, the red curves show the 3rd, 50th, and 97th percentiles for all giants. We interpret stars with v_{broad} larger than the 97th percentile value for their $\log g$ as being rapid rotators. Notably, Li-rich RGB stars are more likely to be rapid rotators than Li-rich RC stars.

stars as they ascend the giant branch (e.g., Carney et al. 2008a). In order to understand how the v_{broad} of a given star differed from the average for their $\log g$, we fitted the overall trend in v_{broad} vs $\log g$ by dividing all giant stars into 100 bins in $\log g$ in the range $0.5 < \log g < 3.2$. In each bin we found the 3rd, 50th and 97th percentile v_{broad} values and then fitted an exponential function of the form $v_{broad} = a \exp(-b \log g) + c$. These functions are shown as the red curves on all panels of Figure 8. We can see that most stars are found with $v_{broad} \approx 8\,\mathrm{km\,s^{-1}}$, so most stars in our sample do not have appreciable rotational velocity.

We interpret stars with v_{broad} above the 97th percentile as being "rapid rotators". In Table 4 are the counts of stars above this threshold. We find that 3.4 per cent (4116/120024) of giants are rapid rotators, slightly higher than predicted for K giants in the field (Carlberg et al. 2011). For just the RC stars, the ratio is 4.9 per cent (2187/44767), while for the RGB it is 2.6 per cent (1929/75257),
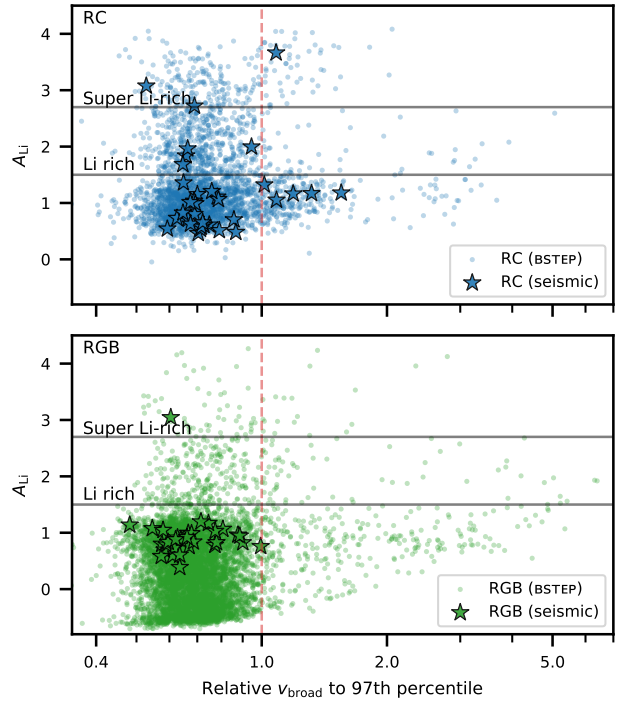

Figure 9. Using the v_{broad}-$\log g$ fits from Figure 8, for each star we calculate the fractional v_{broad}, relative to 97th percentile for their $\log g$. On this scale, e.g., stars with values > 1 have v_{broad} greater than the 97th percentile. We show this for the distributions of the red clump (top panel) and red giant branch (bottom panel) samples. As in Figure 4 in each panel we highlight stars asteroseismically classified as RC or RGB. RC stars are found in a smaller range of fractional v_{broad} than RGB stars, with most below 2. The rapid rotators among the Li-rich RC stars are mostly super Li-rich.

Table 4. Comparison of how many RC and RGB stars are rapid rotators. Rapid rotators are defined as those stars with v_{broad} above the 97th percentile for their $\log g$. RC stars are about twice as likely as RGB stars to be rapid rotators (4.9 per cent versus 2.6 per cent), but the proportion of Li-rich stars that are rapid rotators is higher for RGB stars than RC stars (21.1 per cent versus 11.7 per cent).

	Total stars	Rapid rotators	Li-rich rapid rotators
All giants	120024	4116 (3.4%)	192 (0.16%; 14.7%)
RC	44767	2187 (4.9%)	104 (0.23%; 11.7%)
RGB	75257	1929 (2.6%)	88 (0.12%; 21.1%)

i.e., RC stars are about twice as likely as RGB stars to be rapid rotators. But if we consider just the Li-rich stars, the proportions are markedly different: of the Li-rich RC stars, 11.7 per cent (104/888) are rapid rotators, but on the Li-rich RGB, 21.1 per cent (88/418) are.

In Figure 9 we explore the relationship between rotation of the stars and A_{Li}. For each star we divide its v_{broad} by the 97th percentile of v_{broad} at its $\log g$, so that in Figure 9 those stars with x axis values > 1 are rapid rotators. For both the RC and RGB populations, the Li-normal stars ($A_{Li} < 1.5$) show a range in this fractional v_{broad}, though the RC stars are more restricted, with only a few above 2. Curiously, the rapid rotators in the RC group are
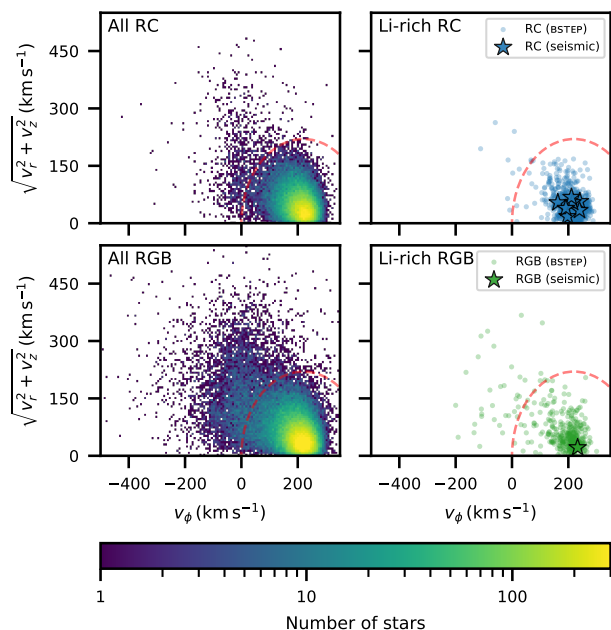
Figure 10. The Galactic orbital velocities presented in the form of Toomre diagrams for (left) all stars in each sample and (right) just Li-rich stars. The top row shows RC stars; the bottom row is RGB. The red dashed circle on all panels indicates the region of this velocity space within which stars have disk-like orbits; stars outside of the circle have orbital velocities typical for a star with a halo orbit. As expected for the GALAH survey selection, most of the stars observed have disk-like orbits, in the lithium-normal and lithium-rich groups.

Figure 11. The J_ϕ vs orbital energy distribution for our stars, with panels arranged the same as in Figure 10. As also shown in Figure 10, the majority of our Li-rich giants have disk-like orbits — i.e., they are largely concentrated on the right edge of the envelope with low eccentricity and in-plane motions ($-2 < E < -1$ and $0 < L_z < 4$). In all panels, the red-dashed rectangle indicates the region of parameter space where stars from the Gaia-Enceladus merger event are found (Koppelman et al. 2018). A handful of our Li-rich RGB stars fall into this box, but their $[\alpha/Fe]$ and age are not consistent with membership to GE.

quite skewed toward being super Li-rich, with only a few RC stars with $1.5 < A_{Li} < 2.7$ being rapid rotators.

Deepak et al. (2020) investigated stellar rotation using the v sin i value reported in GALAH DR2. They also noted that rotation rate increases with decreasing gravity, but did not note anything of interest comparing the Li-rich giants to the Li-normal giants of any of the cohorts they considered. This would be a reasonable interpretation of our results as well: while Li-rich RGB stars are distinctly more likely to be rapid rotators than Li-rich RC stars, they do not generally have larger v_{broad} values than Li-normal RGB stars.

3.4   Spatial and orbital properties

The spatial and orbital properties of our lithium-rich giants follow reasonably with what might be expected from the metallicity distribution. The GALAH+ survey primarily samples the disk of the Milky Way, with only one per cent of the giants stars in the halo (De Silva et al. 2015). The location of the Li-rich giants, both the RC and RGB stars, is consistent with them being a relatively young population in the disk of the Galaxy, with very few found more than 1 kpc out of the plane.

Figure 10 shows Galactocentric rotational velocity versus perpendicular velocity (i.e., a Toomre diagram). The red circle shows the point where the total velocity relative to the Local Standard of Rest is 220 km s^{-1}, which is a canonical division between the disk and the halo (Bonaca et al. 2017). In our data set, red clump stars as a whole are more likely to be on disk-like orbits than halo-like orbits, and very few of the Li-rich RC stars are on halo-like orbits. This is consistent with our picture of RC stars being a younger pop-
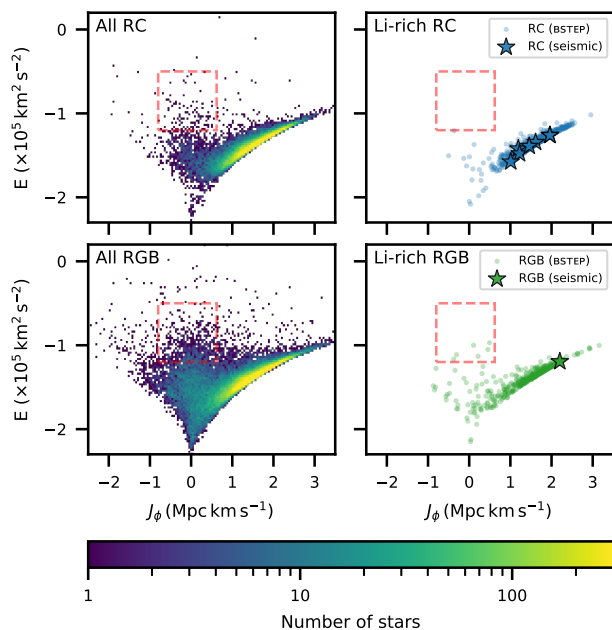
ulation, and with the smaller volume they sample. The majority of RGB stars in our data set also orbit in the disk, but both Li-normal and Li-rich RGB stars are more likely to be on halo-like orbits than RC stars are.

Figure 11 shows the orbital energy E and the azimuthal action J_ϕ, which is the same as the vertical angular momentum L_z. This is a coordinate space in which prograde orbits are on the right side of the plot and retrograde orbits are on the left. The majority of stars in our data set, which follow disk-like orbits, form the highly populated right-hand envelope of the distribution. This confirms the picture from Figure 10 that most of our Li-rich stars are found in the disk of the Milky Way — there are few Li-rich giants in orbits with high energy relative to their angular momentum, or with nonrotating or retrograde orbits.

The red rectangle in Figure 11 highlights the region of this parameter space occupied by the remnant of the Gaia-Enceladus merger event (Helmi et al. 2018; Koppelman et al. 2018). There are a handful of Li-rich stars located in this region of kinematic space. The red clump stars do overlap in $[\alpha/Fe]$-$[Fe/H]$ space with Gaia-Enceladus stars (Monty et al. 2019), but the red giant branch stars do not. In both subsets, the ages we derive for these stars from BSTEP are too young for them to have been captured into the halo as part of Gaia-Enceladus, since that event is thought to have been > 10 Gyr ago (Belokurov et al. 2020a; Chaplin et al. 2020). As such, we do not have evidence for any of our Li-rich giants having extra-Galactic origins.

3.5 Binarity

Recent works have presented two models involving binary stars to explain lithium enrichment on the red clump. Casey et al. (2019) used a large set of lithium-rich giants from the LAMOST survey to argue that the distribution of lithium-rich giants in evolutionary phase requires independent processes operating on the first-ascent giant branch and after the helium flash, based on the lithium depletion timescale. Their proposed mechanism in red clump stars is tidal spin-up from a binary companion driving internal mixing and therefore lithium production via the Cameron-Fowler mechanism. In contrast, Zhang et al. (2020) proposed that Li-rich RC stars are the result of a merger of a RGB-white dwarf binary system.

These hypotheses are in principle testable by searching for binary companions (or lack thereof) in lithium-rich giants through variability in radial velocity, photometry and astrometry. Unfortunately we are not able to draw any significant conclusions on binarity in our data set.

For the the representative binary of Casey et al. (2019) — a 1.5 solar mass giant and a 1.0 solar mass dwarf in a 279-day orbit — we might expect variations of the order of ~ 30 m s^{-1} (as modelled by ELLC, Maxted 2016). This is beyond the precision of HERMES, nor do we have the necessary observational cadence. Price-Whelan et al. (2020) identified about 19,635 candidate binaries in the APO-GEE survey based on radial velocity variations between multiple observations. Of these 66 were in our GALAH+ DR3 giant star data set, including 20 of our RC stars — one of which is Li-rich. It has only three observations with APOGEE, indicating an RV range of ~ 50 km s^{-1}.

In terms of photometric signatures of binarity in the form of transits, assuming random orbital inclinations and observed orbital period distributions (e.g., Raghavan et al. 2010), 2.5 ± 0.5 per cent of our Li-rich RC stars should be in eclipsing binary systems. The secondary will only block about 1 per cent of the disk of the primary with an eclipse period of ~ 3 days. This does not require a very high cadence in photometric monitoring, but none of our Li-rich RC stars have light curves in ASAS-SN (Kochanek et al. 2017) or *TESS* (Ricker et al. 2014) that show evidence for eclipses.

The astrometry from *Gaia* is precise enough to measure the motion of the photocentre of some binary systems (depending on heliocentric distance and the binary properties). The model assumption underlying the data processing for *Gaia* DR2 is that sources are single objects, and if there are photocentre shifts in binary systems these are interpreted as larger than expected astrometric errors. Work by Penoyre et al. (2020) and Belokurov et al. (2020b) have used the Renormalized Unit Weight Error (RUWE), an astrometric error metric reported by *Gaia*, to identify possible binaries. Our data set excludes stars with large RUWE by construction (it is part of flag_sp), because parallax is an important prior in our stellar parameter determination.

3.6 Infrared excess

A fraction of Li-rich RGB stars have been reported to have excess flux in their SED in the infrared, which has been postulated as a sign of a physical connection between lithium production and mass loss. This can be seen in photometry from the IRAS satellite (e.g., Fekel & Watson 1998) and from *WISE*, though its wavelength coverage does not reach as far into the infrared. A close investigation by Rebull et al. (2015) found that the majority of lithium-rich giants in the literature with reported infrared excesses were artifacts in the *WISE* catalog or cases of source confusion. However, they do
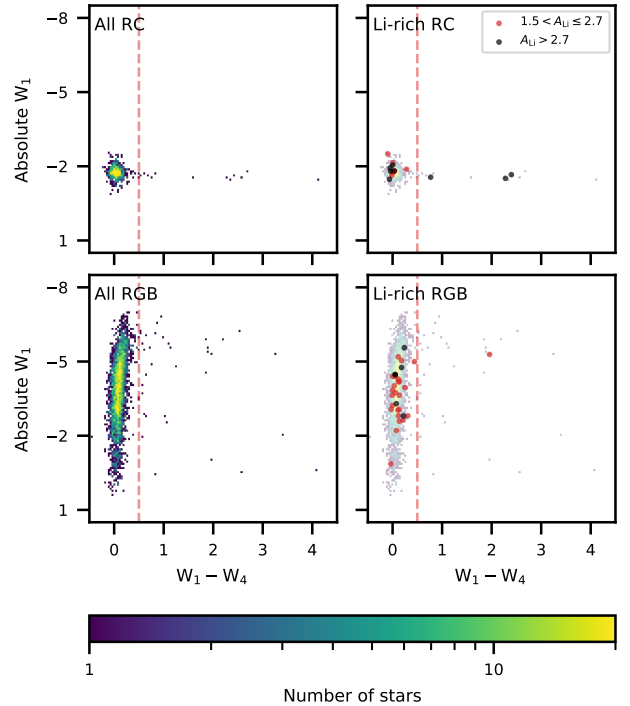

Figure 12. The infrared colour-magnitude diagram for stars in our data set with reliable WISE photometry, showing (top row) RC stars, (bottom row) RGB stars, and (left column) all stars in each sample and (right column) just Li-rich stars. The vertical line at $W_1 - W_4 > 0.5$ indicates stars with an infrared excess. The vast majority of stars show no such excess, but there are a handful of stars that do. The proportion of Li-rich stars that show IR excess (4/49; 8 per cent) is higher than that of the general population of giants (49/4347; 1 per cent).

confirm some as real cases of infrared excess, and they do find that the stars with the largest infrared excess are lithium-rich K giants.

Within our data set (Figure 12), there are only 4349 giants with clean *WISE* detections (those with the cc_flags confusion flag set to 0000 and the ph_qual photometric quality flag set to A for W_1 and W_4), of which only 46 are Li-rich. Overall only a few stars have large infrared colours (defined as $W_1 - W_4 > 0.5$): 49 of the 4349 giants (1 per cent). Of the 46 Li-rich giants with useful WISE photometry, four have large infrared colours (8 per cent). Only one of these is an RGB star, located near the top of the giant branch. The other three have been classified as RC stars, and all three are super Li-rich stars.

In our data set, the stars (both Li-normal and Li-rich) with the largest infrared colours are located on the upper RGB and at the RC. This suggests that infrared excess and mass loss are related, since the top of the RGB is the stage at which the star's atmosphere is extended, cool, and likely to be lost. The red clump is the immediate next step in stellar evolution, and so it is reasonable that we find RC stars that appear to have surrounding material lost during the late RGB. Lithium-rich giants are more likely to have infrared excess than lithium-normal giants, but it is unclear what the directionality of the connection between lithium enrichment and mass loss would be.

3.7 Super lithium-rich stars

In our discussion and figures so far we have been making a distinction between lithium-rich stars, which have $A_{Li} > 1.5$, and super lithium-rich stars, which sit above the primordial abundance of $A_{Li} = 2.7$. For lithium enrichment models that involve adding pristine gas to an evolved star to raise its abundance, this is an important distinction: such mechanisms could only raise a star's abundance toward the primordial value but could not exceed it.

For lithium enrichment models that posit the production of lithium within a star, this distinction is less important, but the question of how to produce as much lithium as is observed does become more difficult to answer at higher lithium abundances. Yan et al. (2018) attempt to model the process for lithium production in the star TYC 429-2097-1, which has an abundance of $A_{Li} = 4.5$. They find that meridional circulation at the RGB bump, where this particular star currently is, is capable of producing more than the observed amount of lithium. The most lithium-rich giant in our data set also has $A_{Li} = 4.5$[2], but as a luminous giant it does not fit within their model.

Super lithium-rich red clump stars in our data set have some interesting properties. While the majority of our super lithium-rich stars are in the red clump phase (Section 2.4), almost none of them are on the secondary red clump, indicating a connection between stellar mass and the ability to produce large amounts of lithium. Also, while the super Li-rich red clump stars are the most rapidly rotating (Fig. 8) and the most metal-rich (Fig. 6), those are two separate groups of stars: the most metal-rich RC stars are not rapidly rotating.

3.8 Summary of observational phenomenology

In this study we explore the properties of 1306 evolved stars from the GALAH survey with elevated lithium abundances ($A_{Li} > 1.5$). We find these main behaviours in the data set:

(i) Red clump stars are more than three times as likely to be lithium-rich as red giant branch stars (Section 2.4);

(ii) The less massive primary RC stars are much more likely than the higher mass secondary RC stars to be super lithium-rich (Section 2.4);

(iii) The occurrence rate of lithium-rich giants with metallicity is markedly different for RC and RGB populations: it increases steadily with metallicity in red clump stars, but it is essentially constant in red giant branch stars below Solar metallicity (Section 3.1);

(iv) Rapidly rotating RGB stars are more like to be lithium-rich than rapidly rotating RC stars (Section 3.3);

(v) Rapidly rotating lithium-rich RC stars tend to be super lithium-rich (Section 3.3).

We recover the changing occurrence rate of lithium-rich giants with metallicity noted by Casey et al. (2019) and the difference between the occurrence rate behaviour in RGB versus RC stars described by Deepak et al. (2020). However, we find a smaller fraction of our Li-rich giants to be RC stars than in Casey et al. (2019). In their LAMOST sample, they classified 80^{+7}_{-6} per cent to be core-helium burning stars, while we find only 68 per cent. Given the sample sizes, this is a significant discrepancy. It is likely a consequence of the difference between the GALAH and LAMOST

selection functions, since LAMOST observes as a conglomerate of multiple simultaneous surveys.

Both rapid rotation and infrared excess show some connection to lithium enrichment, in that lithium-rich stars are more likely to have those properties than lithium-normal stars do. However, the majority of lithium-rich stars do not exhibit either of these features.

4 THE ORIGINS OF LITHIUM ENRICHMENT IN EVOLVED STARS

The broad strokes of the proposed explanations for how a small fraction of evolved stars have come to be enriched in lithium have not changed substantially since the first lithium-rich giant was identified in 1940. Models posit either some external reservoir of lithium (ingestion of a planet or sub-stellar companion, or mass transfer from an AGB companion) or some internal production channel (internal mixing driven by the RGB bump, the He flash, rotation, or binary interactions). The consensus from observational studies, especially those with large data sets, is that there must be multiple processes at work.

The correspondence in red clump stars between rapid rotation and the highest levels of lithium enrichment implies quite strongly that internal mixing processes are capable of driving lithium production. At the same time, Li-rich RGB stars are nearly twice as likely as Li-rich RC stars to be rapidly rotating, indicating that rotationally driven internal mixing plays a larger role in Li production on the RGB than on the RC.

For stars on the red giant branch, we find that there is a concentration of Li-rich stars near the RGB bump, which can be explained as a result of internal mixing triggered by a change in internal structure. We also find Li-rich stars at all points on the RGB, at all metallicities and ages. The occurrence rate for Li-rich RGB stars is essentially flat for all subsolar metallicities and dramatically higher at supersolar metallicity. This suggests either two independent lithium enrichment processes for RGB stars, or one process that is strongly suppressed at low metallicity. A metallicity-independent lithium enrichment process on the RGB is somewhat incompatible with planet engulfment models, since that process should be more common in metal-rich stars, where the planet occurrence rate is higher. Further abundance studies focused on boron and beryllium could shed some light on this problem, since they have similar burning temperatures to lithium and should be co-accreted with it from planets.

As in previous studies, the majority of our lithium-rich giants are red clump stars, and this requires a lithium enrichment process triggered at or after the helium flash. The fact that the occurrence rate for RC stars rises steadily with increasing metallicity may be a result of the fact that the time spent on the red clump is longer at higher metallicity, or it may reflect a more effective internal mixing in high metallicity giant stars because of their less compressed interior structure, or it may be driven by a higher binary fraction (with the correct mass ratio and orbital separation) at higher metallicity. These possibilities will need to be evaluated through careful modeling of stellar structure, evolution, and star formation. We cannot comment directly on binary interactions as the driver for internal mixing from our data set, but this is an avenue for future work that may clarify the situation significantly.

---

[2] See Section 2.3 for discussion about our inability to identify stars with $A_{Li} > 4.6$.

References

Aguilera-Gómez C., Chanamé J., Pinsonneault M. H., Carlberg J. K., 2016, ApJ, 829, 127
Asplund M., Grevesse N., Sauval A. J., Scott P., 2009, ARA&A, 47, 481
Astropy Collaboration et al., 2018, AJ, 156, 123
Bailer-Jones C. A. L., Rybizki J., Fouesneau M., Mantelet G., Andrae R., 2018, AJ, 156, 58
Bedding T. R., et al., 2011, Nature, 471, 608
Belokurov V., Sanders J. L., Fattahi A., Smith M. C., Deason A. J., Evans N. W., Grand R. J. J., 2020a, MNRAS
Belokurov V., et al., 2020b, preprint (`arXiv:2003.05467`)
Bonaca A., Conroy C., Wetzel A., Hopkins P. F., Kereš D., 2017, ApJ, 845, 101
Buder S., et al., 2018, MNRAS, 478, 4513
Burbidge E. M., Burbidge G. R., Fowler W. A., Hoyle F., 1957, Reviews of Modern Physics, 29, 547
Cameron A. G. W., Fowler W. A., 1971, ApJ, 164, 111
Carlberg J. K., Majewski S. R., Patterson R. J., Bizyaev D., Smith V. V., Cunha K., 2011, ApJ, 732, 39

Carlberg J. K., Cunha K., Smith V. V., Majewski S. R., 2012, ApJ, 757, 109
Carney B. W., Latham D. W., Stefanik R. P., Laird J. B., 2008a, AJ, 135, 196
Carney B. W., Gray D. F., Yong D., Latham D. W., Manset N., Zelman R., Laird J. B., 2008b, AJ, 135, 892
Casey A. R., et al., 2016, MNRAS, 461, 3336
Casey A. R., et al., 2019, ApJ, 880, 125
Caswell T. A., et al., 2020, Matplotlib/Matplotlib v3.1.3
Chaplin W. J., et al., 2020, Nature Astronomy
Charbonnel C., Balachandran S. C., 2000, A&A, 359, 563
Cui X.-Q., et al., 2012, Research in Astronomy and Astrophysics, 12, 1197
Cyburt R. H., Fields B. D., Olive K. A., 2008, J. Cosmology Astropart. Phys., 2008, 012
De Silva G. M., et al., 2015, MNRAS, 449, 2604
Deepak Reddy B. E., 2019, MNRAS, 484, 2000
Deepak Lambert D. L., Reddy B. E., 2020, MNRAS, 494, 1348
Denissenkov P. A., 2012, ApJ, 753, L3
Fekel F. C., Watson L. C., 1998, AJ, 116, 2466
Fields B. D., Olive K. A., Yeh T.-H., Young C., 2020, J. Cosmology Astropart. Phys., 2020, 010
Gaia Collaboration et al., 2016, A&A, 595, A1
Gaia Collaboration et al., 2018, A&A, 616, A1
Gamow G., Landau L., 1933, Nature, 132, 567
Gao Q., Shi J.-R., Yan H.-L., Yan T.-S., Xiang M.-S., Zhou Y.-T., Li C.-Q., Zhao G., 2019, ApJS, 245, 33
Gilmore G., et al., 2012, The Messenger, 147, 25
Girardi L., 2016, ARA&A, 54, 95
Gonzalez O. A., et al., 2009, A&A, 508, 289
Gratton R. G., Sneden C., Carretta E., Bragaglia A., 2000, A&A, 354, 169
Gustafsson B., Edvardsson B., Eriksson K., Jørgensen U. G., Nordlund Å., Plez B., 2008, A&A, 486, 951
Hansen T. T., Andersen J., Nordström B., Beers T. C., Placco V. M., Yoon J., Buchhave L. A., 2016, A&A, 588, A3
Helmi A., Babusiaux C., Koppelman H. H., Massari D., Veljanoski J., Brown A. G. A., 2018, Nature, 563, 85
Hon M., Stello D., García R. A., Mathur S., Sharma S., Colman I. L., Bugnet L., 2019, MNRAS, 485, 5616
Hunter J. D., 2007, Computing in Science & Engineering, 9, 90
Iben I., 1965, ApJ, 142, 1447
Karaali S., Bilir S., Gokce E. Y., Plevne O., 2019, Publ. Astron. Soc. Australia, 36, e040
Karakas A. I., Lugaro M., 2016, ApJ, 825, 26
Kirby E. N., Fu X., Guhathakurta P., Deng L., 2012, ApJ, 752, L16
Kirby E. N., Guhathakurta P., Zhang A. J., Hong J., Guo M., Guo R., Cohen J. G., Cunha K., 2016, ApJ, 819, 135
Kochanek C. S., et al., 2017, PASP, 129, 104502
Koppelman H., Helmi A., Veljanoski J., 2018, ApJ, 860, L11
Kos J., et al., 2017, MNRAS, 464, 1259
Kraft R. P., Peterson R. C., Guhathakurta P., Sneden C., Fulbright J. P., Langer G. E., 1999, ApJ, 518, L53
Lagarde N., et al., 2019, A&A, 621, A24
Lewis I. J., et al., 2002, MNRAS, 333, 279
Lind K., Primas F., Charbonnel C., Grundahl F., Asplund M., 2009, A&A, 503, 545
Mainzer A., et al., 2011, ApJ, 731, 53
Marigo P., et al., 2017, ApJ, 835, 77
Martell S. L., Shetrone M. D., 2013, MNRAS, 430, 611
Maxted P. F. L., 2016, A&A, 591, A111
McKellar A., 1940, PASP, 52, 407
McKellar A., 1941, The Observatory, 64, 4
Monty S., Venn K. A., Lane J. M. M., Lokhorst D., Yong D., 2019, preprint (`arXiv:1909.11969`)
Mosser B., et al., 2012, A&A, 548, A10
Penoyre Z., Belokurov V., Evans N. W., Everall A., Koposov S. E., 2020, preprint (`arXiv:2003.05456`)
Pilachowski C. A., Sneden C., Kraft R. P., Harmer D., Willmarth D., 2000, AJ, 119, 2895
Piskunov N., Valenti J. A., 2017, A&A, 597, A16

Plevne O., Önal Taş Ö., Bilir S., Seabroke G. M., 2020, ApJ, 893, 108

Price-Whelan A., Sipocz B., Lenz D., Major S., Oh S., 2018, adrn/gala: v0.3, doi:10.5281/zenodo.1227457

Price-Whelan A. M., et al., 2020, preprint (arXiv:2002.00014)

Raghavan D., et al., 2010, ApJS, 190, 1

Ramírez I., Fish J. R., Lambert D. L., Allende Prieto C., 2012, ApJ, 756, 46

Rebull L. M., et al., 2015, AJ, 150, 123

Ricker G. R., et al., 2014, Journal of Astronomical Telescopes, Instruments, and Systems, 1, 014003

Salpeter E. E., 1955, Physical Review, 97, 1237

SciPy 1.0 Contributors et al., 2020, Nature Methods

Sharma S., et al., 2018, MNRAS, 473, 2004

Sharma S., et al., 2019, MNRAS, 490, 5335

Sheinis A., et al., 2015, Journal of Astronomical Telescopes, Instruments, and Systems, 1, 035002

Silva Aguirre V., et al., 2020, ApJ, 889, L34

Singh R., Reddy B. E., Bharat Kumar Y., Antia H. M., 2019, ApJ, 878, L21

Smiljanic R., et al., 2018, A&A, 617, A4

Stassun K. G., et al., 2019, AJ, 158, 138

Stello D., et al., 2013, ApJ, 765, L41

Stello D., et al., 2017, ApJ, 835, 83

Trimble V., 1975, Reviews of Modern Physics, 47, 877

Trimble V., 1991, A&ARv, 3, 1

Valenti J. A., Piskunov N., 1996, A&AS, 118, 595

Vrard M., Mosser B., Samadi R., 2016, A&A, 588, A87

Wallerstein G., Conti P. S., 1969, ARA&A, 7, 99

Wallerstein G., Sneden C., 1982, ApJ, 255, 577

Wittenmyer R. A., et al., 2018, AJ, 155, 84

Wright E. L., et al., 2010, AJ, 140, 1868

Yan H.-L., et al., 2018, Nature Astronomy, 2, 790

Zhang X., Jeffery C. S., Li Y., Bi S., 2020, ApJ, 889, 33

This paper has been typeset from a TeX/LaTeX file prepared by the author.